Giant Ultrafast All-Optical Modulation Based on Exceptional Points in Exciton–Polariton Perovskite Metasurfaces

Mikhail A. Masharin, Tatiana Oskolkova, Furkan Isik, Hilmi Volkan Demir,** Anton K. Samusev, and Sergey V. Makarov**

ACCESS | Metrics & More | Article Recommendations | SI Supporting Information

ABSTRACT: Ultrafast all-optical modulation with optically resonant nanostructures is an essential technology for high-speed signal processing on a compact optical chip. Key challenges that exist in this field are relatively low and slow modulations in the visible range as well as the use of expensive materials. Here we develop an ultrafast all-optical modulator based on $MAPbBr_3$ perovskite metasurface supporting exciton–polariton states with exceptional points. The additional angular and spectral filtering of the modulated light transmitted through the designed metasurface allows us to achieve 2500% optical signal modulation with the shortest modulation time of 440 fs at the pump fluence of ∼40 $\mu J/cm^2$. Such a value of the modulation depth is record-high among the existing modulators in the visible range, while the main physical effect behind it is polariton condensation. Scalable and cheap metasurface fabrication via nanoimprint lithography along with the simplicity of perovskite synthesis and deposition make the developed approach promising for real-life applications.
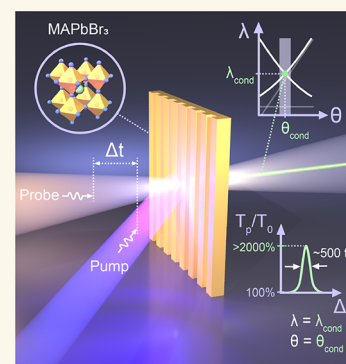
INTRODUCTION

Light modulation and control upon external stimulus are highly important for a wide range of technologies including telecommunication, detection, imaging, and even biomedical applications. The key parameters used to characterize an optical modulator are modulation depth and speed as well as power consumption. Such optical modulation methods as electro-optic modulation face some limitations in terms of speed, energy consumption, and cross-talk, making it challenging to apply for efficient ultrafast optical signal modulator.[1,2] In turn, nonlinear all-optical modulators offer inherent benefits including faster operating speeds and lower heat generation.[3−5] This approach employs an intensive light pulse working as a control beam that induces nonlinear optical effects in the material to control the propagation of a weak signal optical pulse. As a result, signal processing can be entirely accomplished in the photonic domain with modulation speeds approaching 1 THz level, making it highly promising for ultrafast optical signal processing.[6,7]

The realization of nanoscale-compact and still efficient all-optical modulators has attracted great attention within the nanophotonics community in recent years because they are even more promising for overcoming the intrinsic speed and heat dissipation limitations of conventional electronics.[2,8,9]

Metallic nanostructures, utilizing plasmons and surface plasmon polaritons to produce ultrafast optical modulation, were developed extensively during the last decades,[10−16] but they possess relatively high losses in the visible and near-IR spectral ranges. In this regard, the all-dielectric approach[17] has an advantage because of the vanishing of linear optical absorption in most cases, motivating the development of nanostructures and metasurfaces for ultrafast modulation.[18,19] Among dielectric and semiconductor modulators based on Si,[20−23] GaAs,[24,25] GaN,[26] and GaP,[27,28] nanophotonic designs demonstrated excellent performance. Some intermediate position between metallic and dielectric materials is held by the systems operating in epsilon-near-zero (ENZ) regime,[29−33] where the strong optical modulation depth up to 8630% with modulation time longer than 1 ps was observed for cadmium oxide,[34] but only in the NIR spectral region. Ultrafast modulators using 2D materials[35−38] including TMDs[39−41]
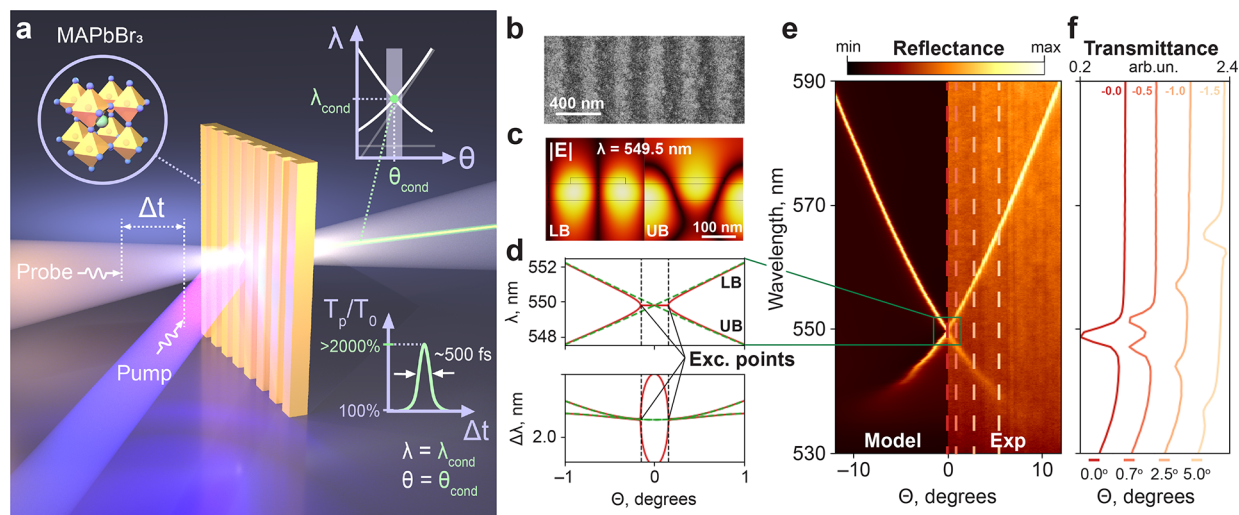
Figure 1. Concept and sample characterization. (a) Conceptual drawing of the experiment and the studied phenomenon of ultrafast optical modulation in the perovskite metasurface. (b) SEM image of the fabricated sample. (c) The calculated normalized field distribution in the unit cell at $\lambda = 549.5$ nm and resonant angle of incidence $\theta = 0$. (d) Calculated eigenvalues of the interacting polariton modes in the vicinity of $\theta = 0$. (e) The modeled and experimentally measured angle-resolved reflectance spectra of the perovskite metasurface at room temperature. (f) Measured linear transmittance spectra of the perovskite metasurface at different angles of incidence, shown by the dashed lines in panel e.

and 2D perovskites[42] are also promising materials due to the simplicity of their integration with planar metasurfaces and nanoantennas as well as strong excitonic response in the visible range, which is sensitive to the excitation conditions. It should be noticed, in the case of the exciton−polariton systems, where the exciton is strongly coupled to the resonant optical cavity mode, there can be demonstrated the strong ultrafast optical modulation based on the stimulated polariton relaxation.[5,43] Moreover, exciton−polariton systems can be even more sensitive to any perturbation if they are coupled with exceptional point photonic states.[44−46]

In this work, we utilize exceptional point states in MAPbBr$_3$ perovskite metasurfaces supporting exciton−polariton condensation for the realization of an ultrafast all-optical modulator. To achieve the 2500% optical signal modulation with the shortest modulation time of about 440 fs, we employ angular-spectral filtering of light undergoing amplitude modulation while being transmitted through the metasurface, as schematically shown in Figure 1a. This modulation depth is a record-high one among the known modulators in the visible range. The underlying mechanism behind it is the ultrafast polariton condensation,[47,48] which is consistent with the previous work for this type of halide perovskites and photon cavity design.[49]

RESULTS

Characterization of the Optical States in the Studied Perovskite Metasurface. The perovskite metasurface based on MAPbBr$_3$ is fabricated by a sequential process comprising spin-coating followed by nanoimprint lithography. The resulting perovskite metasurface on a silica substrate represents one-dimensional grating characterized by a periodicity of 320 nm, a grating height of 72 nm, a modulation depth of 20 nm, and a comb width of 167 nm. Figure 1b shows a scanning electron microscopy (SEM) image of the aforementioned sample. The vertical characteristics of this structure are ascertained through atomic force microscopy (AFM) and are described in the Supporting Information (SI).

The optical eigenmodes and electric field distribution of the metasurface are computed through numerical simulations (see Methods for details), incorporating the extracted grating parameters and the refractive index dispersion of the material.[50] Notably, at the normal angle of incidence $\theta = 0$ (Figure 1c), the resonant states of the antisymmetric upper branch (UB) and the symmetric lower branch (LB) coincide precisely at $\lambda = 549.5$ nm. This convergence of the two counterpropagating modes is also evident in both numerically modeled (see Methods for details) and experimentally measured angle-resolved reflectance spectra (Figure 1e). Consequently, in the transmission spectra obtained at various incident angles, instead of observing resonance peaks in reflection, we observe corresponding dips (Figure 1f). Building upon our prior research and numerical modeling, it is worth noting that variations in the comb width result in the splitting of modes into a high-Q bound state in the continuum (BIC) and low-Q guided-mode resonance. When the comb width is substantially less than half the period of the structure, the BIC is observed at the frequencies above the crossing point, whereas it shifts below the latter when the comb width exceeds the half-period.[51]

The presence of room-temperature excitons in MAPbBr$_3$[52] along with the strong optical field confinement (Figure 1c) enables the realization of a strong light-matter coupling regime, which is described in detail in the SI. Previous research also has demonstrated the existence of exciton−polaritons in similar structures.[49,53,54] Namely, in such systems, the behavior of the interaction of the modes can be described via Hamiltonian:[55]

$$\hat{H}(\theta) = \begin{pmatrix} E_+(\theta) & U \\ U & E_-(\theta) \end{pmatrix} - i \begin{pmatrix} \gamma_{nr}(\theta) + \gamma_r & \gamma_r \\ \gamma_r & \gamma_{nr}(\theta) + \gamma_r \end{pmatrix}$$

(1)

where $E_{+,-}(\theta)$ are the real parts of the mode eigenvalues with positive and negative group velocity, respectively, which can be found as the spectral mode position. The parameters $\gamma_{nr,r}$ delineate the optical losses stemming from nonradiative and
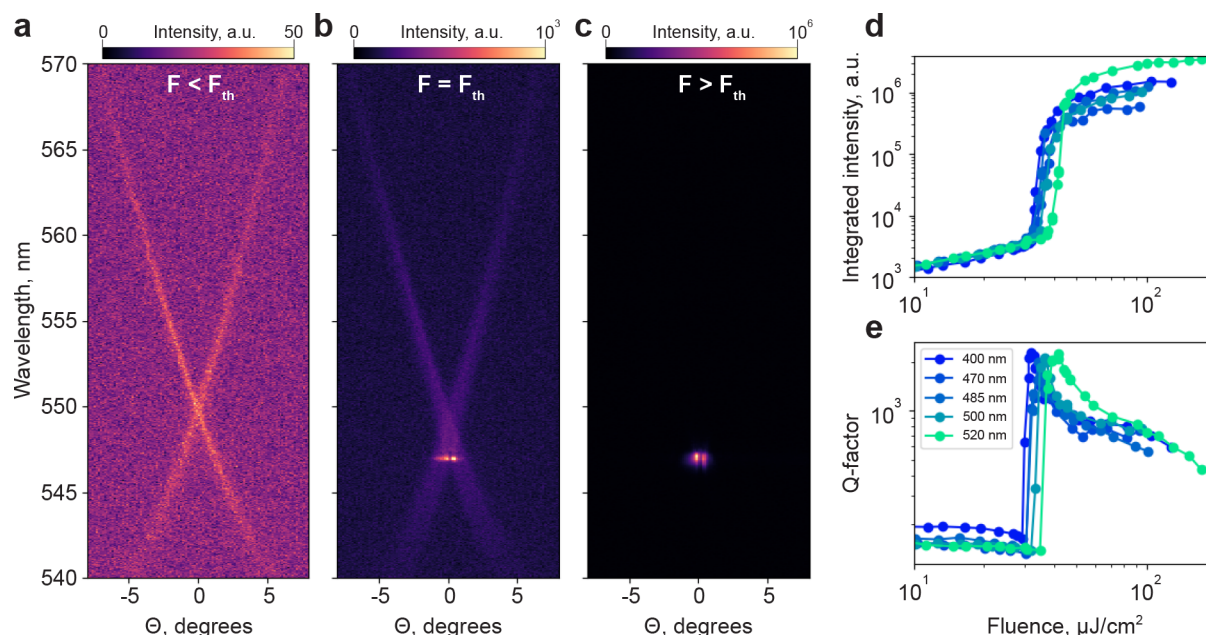
Figure 2. Pump fluence-dependent emission measurements. (a−c) Angle-resolved emission spectra of perovskite metasurface for the pump fluence below, equal, and above the lasing threshold. (d, e) The intensity and Q-factor of the emission as a function of the pump fluence at different pump wavelengths.

radiative processes. The total loss rate, represented by $\gamma(\theta) = \gamma_{nr}(\theta) + \gamma_r$, characterizes the imaginary parts of the states' energies and corresponds to the spectral line width of the modes. The parameter U quantifies the coupling strength between the counterpropagating modes and dictates the splitting in the spectral vicinity of the modes' intersection. In general, the interaction lies in the complex field, which means that the eigenmode splitting appears in both the real and imaginary parts. Tuning the geometry of the metasurface it is possible to change both leaky mode dispersions and coupling coefficient U. In a previous study, we demonstrated that applying a nonresonant optical pump to such structures induces optical gain, reducing nonradiative losses. This effect can lead to the degeneracy of the real and imaginary parts of the eigenmodes near $\theta = 0$, which is referred to as the exceptional points (Figure 1d).[49]

Wavelength- and Fluence-Dependent Angle-Resolved Emission Measurements. The spontaneous emission spectra of MAPbBr$_3$ in its polycrystalline thin film or single crystal forms, observed at room temperature, typically exhibit a peak at around 530 nm. This peak is slightly red-shifted from the exciton resonance.[56,57] However, in the MAPbBr$_3$ metasurface under study, the emission is centered around 550 nm and confined within the optical modes, as depicted in Figure 2a. This phenomenon arises from the strong coupling between exciton and leaky modes. It is worth noting that there is still observable uncoupled, nondirectional photoluminescence (PL) emission occurring around 530 nm. However, it is significantly less intense when compared to the emission associated with the leaky modes (see SI for details).

Applying the nonresonant femtosecond optical pump to the studied perovskite metasurface at the fluences below 30 μJ/cm^2, the linear regime of PL emission is observed (Figure 2a). As the pump fluence is progressively increased, reaching threshold values in the range of 30−40 μJ/cm^2, narrow intense laser emission occurs with high directivity in the vicinity of $\theta = 0$, as illustrated in Figure 2b. As the fluence surpasses the

threshold, the laser emission further intensifies and broadens across the spectrum, as indicated in Figure 2c. The emission is associated with the formation of an exciton−polariton condensate driven by exceptional points, a phenomenon comprehensively investigated previously.[49]

The optical nonresonant pump means that the energy of the incident photons exceeds the uncoupled exciton energy. When a photon is absorbed, the carriers cross over the bandgap with some excess energy, which is generally determined by the difference between the bandgap and the photon energy (or wavelength). Subsequently, the excited electrons and holes scatter through the phonons, dissipating the excess energy and forming excitons. In this sense, the time required for the excited electrons and holes to relax to the energy states of excitons and exciton−polaritons is strongly dependent on the pump wavelength. In essence, shorter pump wavelengths cause more delay time for these relaxation processes. However, shorter wavelengths correspond to higher absorption by the material in the blue spectral region, resulting in a larger number of excited carriers when compared with lower pump photon energy.

To experimentally explore the impact of the pump wavelength on the lasing, we conducted fluence-dependent measurements at various pump wavelengths, as presented in Figure 2d and e. Note that the angle-resolved spectra, as depicted in Figure 2a−c, exhibit no qualitative changes at different pump wavelengths and therefore are omitted from the text. In the light−light curves (Figure 2d), we observe an increase in the pump threshold for longer pump wavelengths due to less efficient absorption by the sample. The Q-factor of the lasing emission reaches values around 2,200 for all studied pump wavelengths. Notably, the intensity of the lasing emission is significantly higher when the pump wavelength is set at 520 nm. This is attributed to the fact that the photon energy at 520 nm falls below the MAPbBr$_3$ bandgap but exceeds the exciton energy, resulting in the excitation of a larger number of excitons. Since in this case there is no
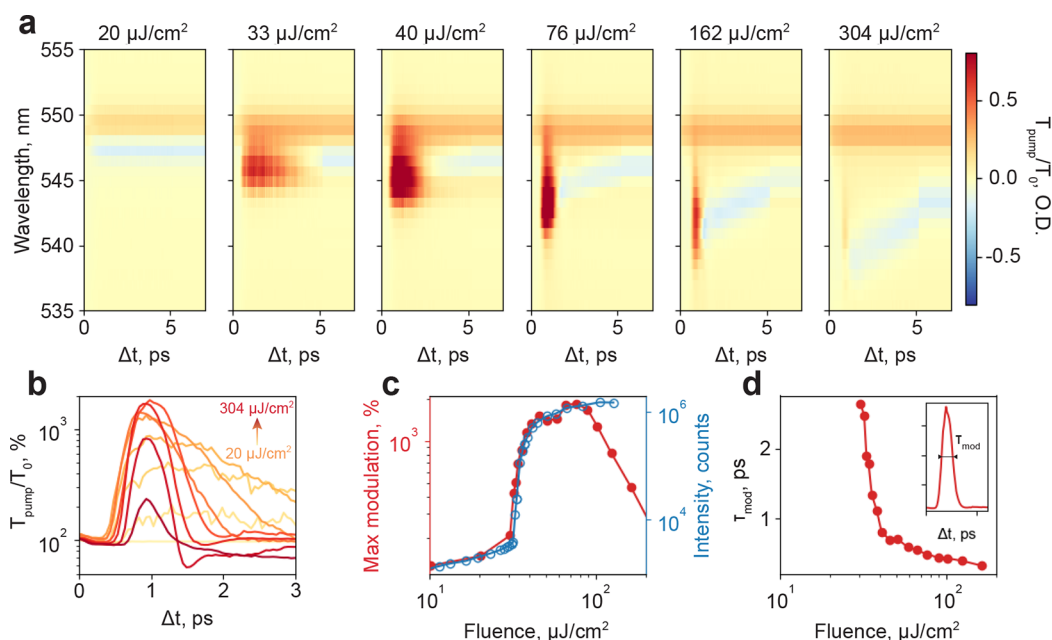
Figure 3. Pump fluence-dependent TTS measurements. (a) The results of the TTS measurements for the 400 nm fs pump at different pump fluences. The pseudocolor shows the ratio of the transmission spectra after the pump pulse and pristine transmission. The x-axis shows the time delay between the probe and pump pulses. (b) Transmission spectra modulation at the polariton condensate wavelength as a function of the time delay at different pump fluences from 20 to 304 μJ/cm^2 (gradient color from yellow to red, respectively). (c) The value of the maximum modulation and lasing emission intensity as a function of the pump fluence. (d) The transmission modulation time depending on the pump fluence. The values were calculated as the full width at half-maximum of the dependencies, shown in panel (b).

conversion from the free electron–hole pairs to excitons, the efficiency of the exciton–polariton generation and, consequently, the intensity of polariton lasing are significantly enhanced.

Transient Transmission Measurements. Stimulated polariton relaxation and polariton condensation offer a highly effective platform for achieving ultrafast optical modulation, as established in prior research.[5,43] To investigate this phenomenon in our system, we conducted transient transmission spectroscopy (TTS) measurements on the perovskite metasurface while systematically varying both the pump fluence and wavelength. In the pursuit of minimizing power consumption, for fluence-dependent TTS measurements, we initially fixed pump wavelength at 400 nm which was confirmed to correspond to the lowest pump fluence threshold for polariton condensation (Figure 2d,e). For the broadband (white) probe pulse, we set the incident angle θ to 0 (surface normal), a configuration where polariton condensation is prominently observed. The linear transmission spectrum in these experiments, denoted as T_0, is represented by the red line in Figure 1f. By introducing a pump pulse with a time delay ΔT relative to the probe pulse, we measured the transmission spectrum labeled as T_{pump}. The ratio of these transmission spectra is plotted as a function of the time delay for various pump fluences in Figure 3a.

Below the pump fluence threshold, we identify the presence of two closely situated spectral features: a bleached band and an absorbed band, both centered on the mode resonance (Figure 3a). These bands originated from the linear polariton blueshift phenomenon, which is contingent upon the carrier concentration within the system, as discussed in detail in prior studies.[58,59] The pumped carriers in the system induce a minor blueshift of the mode resonance toward shorter wavelengths, manifesting as the bleached band (red region) at the original

spectral position and the absorbed band (blue region) at the shifted position. It is noteworthy that the time scale associated with this linear blueshift aligns with the exciton bleaching band (see Figure S4 for details).

Upon increasing the pump fluence to threshold values, a pronounced bleaching effect becomes evident in the blue-shifted mode, characterized by its short duration, narrow spectral range, and strong intensity in comparison to the exciton bleaching in the vicinity of 525 nm (see SI for details). This phenomenon is associated with the emergence of polariton condensation. Notable, we observe a discernible time delay (τ_{delay}) of approximately 1 ps following the absorption of the pump pulse before polariton condensation is formed (Figure 3b). This time delay reflects the duration required for the excited carriers to relax down to the energy states associated with exciton–polaritons, ultimately forming the polariton condensate. In the resulting data set, we estimate the modulation lifetime (τ_{mod}) by quantifying the full time width at half-maximum of the optical modulation at the polariton condensate wavelength as a function of pump fluence.

With further increasing 400 nm pump fluence, the maximum of the optical modulation experiences significant growth, reaching values up to 2000% of the linear transmission (Figure 3c), while the modulation lifetime (τ_{mod}) shortens. The increase of the maximum optical modulation can be attributed to polariton accumulation in the condensed state. However, at the highest pump fluences, the appearance of abnormally high optical gain disrupts the conditions necessary for exceptional points, leading to the disappearance of polariton condensation and transmission modulation.[49] In turn, the reduction of τ_{mod} is attributed to the fact that stimulated polariton relaxation is a nonlinear process, with its rate scaling proportionally to the square of the polariton concentration.[60,61] This nonlinear
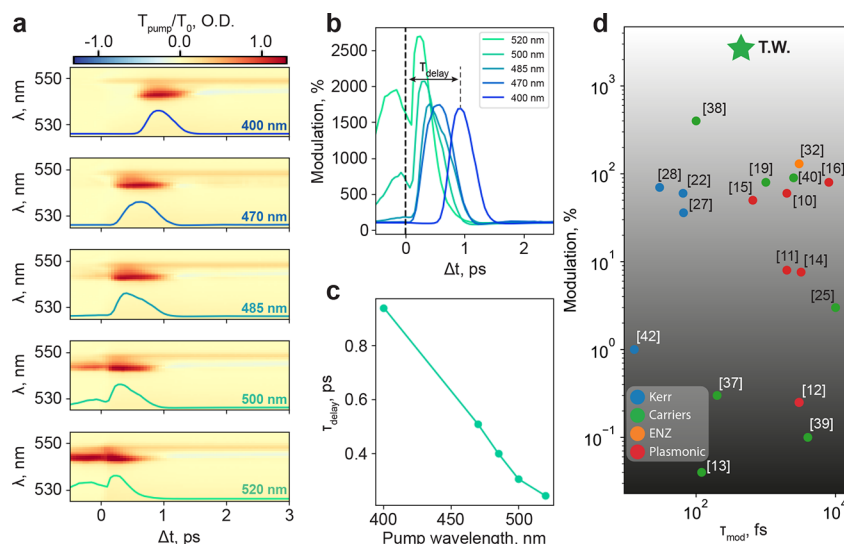
Figure 4. Pump wavelength-dependent TTS measurements. (a) Results of TTS measurements for different pump wavelength at 70 $\mu J/cm^2$. (b) Transmission modulation at the condensate wavelength at 70 $\mu J/cm^2$ pump fluence and various pump wavelengths. (c) Time delay to the optical modulation as a function of the pump wavelength. (d) Maximum modulation values as a function of the time modulation in the visible spectral range: a comparison of the previously published results with the results of this work (T.W.).

scaling results in an accelerated stimulated polariton relaxation rate to the condensed state and, consequently, a reduction in the modulation time with an increasing pump fluence, as shown in Figure 3d. At the point of maximum transmission modulation, τ_{mod} is observed to be equal to 440 fs. Moreover, τ_{delay} does not depend on the pump fluence, indicating that the number of excited carriers does not significantly impact the relaxation rate of the free carriers.

It should be noted that as the pump fluence increases, there is an observed blueshift of the polariton mode (bleached band in Figure 3a). This phenomenon corresponds to the nonlinear polariton blueshift, widely observed and extensively studied in exciton−polariton systems, including those based on halide perovskites.[59,61−63] Unfortunately, the spectral resolution of the used setup does not allow for the precise measurement of the blueshift amount as a function of the pump fluence. However, we have made an approximate estimation of the polariton nonlinear blueshift time scale, which is given in Figures S5 and S6. The time scale associated with the nonlinear polariton blueshift typically falls within the range of 5−10 ps, notably shorter than the time scale observed for the transmission modulation caused by polariton condensation.

Such short modulation time, as well as high modulation depth, are achieved thanks to the high sensitivity of the exceptional points to the external perturbation, in particular, to the nonlinear polariton blueshift and optical gain. Further, the exceptional points appear at the wavelengths in the vicinity of mode crossing, which can be tuned by the design of the metasurface, granting spectral tunability to the optical modulator. Finally, the Purcell factor associated with the exceptional points enables a reduced condensation pump threshold,[64] allowing for the use of lower control pulse power.

To assess the validity of our hypothesis on the relationship between excess carrier energy and τ_{delay} of the polariton condensation, we conducted TTS measurements with varying pump wavelength. Similar to our pump fluence-dependent measurements at 400 nm, we observed robust optical modulation above the fluence threshold for different pump wavelengths. Qualitatively, the behavior of the pump fluence-

dependent TTS results remains consistent across all pump wavelengths (see SI for details). To study the impact of the pump wavelength, we compare the results of TTS measurements conducted at a fixed fluence of 70 $\mu J/cm^2$, which corresponds to the maximum transmission modulation, shown in Figure 4a.

The transmission modulation attains its maximum values, reaching 2550% at a pump wavelength of 520 nm. This heightened modulation results from more efficient pumping of exciton−polariton condensation, as also evidenced in the lasing measurements (Figure 2d). Notably, the experimental results reveal a shift in the optical modulation over time as the pump wavelength increases. This temporal shift corresponds to a reduction in the time delay required for the condensation τ_{delay} (Figure 4b). The values of τ_{delay} extracted for all pump wavelengths are presented in Figure 4c, starting from 0.90 ps at 400 nm and falling to 0.24 ps at 520 nm. As previously discussed, this effect is attributed to the diminishing requirement for excess energy of the free carriers to relax before forming exciton and exciton−polariton states. The difference between the average excess energy and τ_{delay} allows us to estimate the relaxation rate of free carriers, which is determined to be around 0.90 eV/ps.

In the resulting TTS data obtained at the pump wavelengths of 500 and 520 nm, one can mention that the transmission modulation commences with negative values of Δt (Figure 4a,b). This phenomenon can be elucidated by the substantial overlap between the probe pulse, pump pulses, and transmission modulation profile. The pump and probe pulses used possess a duration of 220 fs, and the modulation profile is governed by τ_{delay} and τ_{mod}. Due to the comparable values of these parameters, the absorbed front part of the pump pulse can induce optical modulation, which thereby influences the backward part of the probe pulse. This interplay results in the observed transmission modulation occurring at "negative" time delays in the TTS data, but in fact, it appeared due to the finite duration of the used pump and probe pulses. The dip in the modulation around $\Delta t = 0$ at 500 and 520 nm is associated with short and relatively weak absorption bands, which can

also be noticed in the linear regime (see Figures S7 and S8 in SI). However, when these absorption bands coincide with the opposing effect of transmission bleaching, they become significantly pronounced in the experimental data (Figure 4b).

CONCLUSION

In summary, we have demonstrated that the perovskite metasurface based on MAPbBr$_3$ provides strong and ultrafast optical modulation based on the polariton condensation mediated by exceptional points at room temperature. The modulation of transmission filtered spectrally and angularly exceeds 2500% of the pristine values thanks to the accumulation of boson exciton—polaritons in a condensed state. The observed modulation time is 440 fs with a minimum control pump fluence of approximately 40 μJ/cm^2. The combination of the relatively short modulation time and high transmission modulation depth is achieved thanks to the benefit features of exceptional points. Taking into account the minimum pump spot of 8.5 μm required to observe polariton condensation, the minimum pulse energy sufficient for the modulation is around 29 pJ/bit. Compared to existing systems, our optical modulator sets a record for the highest transmission modulation depth in the visible spectral range at the moment while exhibiting comparable time modulation values and control pump power consumption. The values of the optical modulation based on polariton condensate are as high as demonstrated with epsilon-near-zero (ENZ) systems in near-infrared spectral region[33,34] (see SI for details). Crucially, the modulation duration and its delay with respect to the pump pulse can be tailored by adjusting the pulse power and wavelength, providing multiple degrees of freedom for various applications.

Note that the observed modulation time is constrained by the pulse widths of the utilized pump and probe and can potentially be reduced in systems with shorter pulses. Furthermore, in perovskite systems based on single crystals, characterized by lower nonradiative losses and lasing pump thresholds,[65] the pump power can be further minimized. In this context, the innovative concept of transmission modulation reliant on the polariton condensates in planar perovskite systems, as demonstrated in this study, holds immense promise as a cost-effective and versatile platform for developing robust ultrafast optical modulators for a wide range of applications.

METHODS

Sample Synthesis. The fabrication process comprises three distinct steps: solution preparation, thin film spin-coating, and nanoimprint lithography. Initially, a perovskite solution was prepared within a dry N$_2$ glovebox by mixing 33.59 mg of MABr (TCI) and 110.1 mg of PbBr$_2$ (TCI). This mixture was then dissolved in a 1 mL solution of DMF and DMSO in a 3:1 ratio and stirred using a magnetic stirrer for 24 h.

Subsequently, SiO$_2$ substrates were meticulously cleaned through successive sonication in deionized water, followed by acetone and 2-propanol, each for a duration of 10 min. Once dried, the substrates were exposed to a oxygen plasma cleaner for 10 min to enhance surface adhesion. These pristine substrates were transferred to the dry N$_2$ glovebox for the subsequent film deposition.

The synthesis of the perovskite film commenced with the deposition of 30 μL of MAPbBr$_3$ solution onto the cleaned substrate. The spin-coating process was initiated, with the substrate being spun for 50 s at a rotational speed of 3,000 rpm. At the 35th second, after the rotation had commenced, 300 μL of the antisolvent (toluene) was

gently added atop the rotating substrate to eliminate excess solution and facilitate rapid and uniform film crystallization.

In the third step, the substrate with the perovskite film, still in an intermediate state prior to thermal annealing, was transferred to a laboratory press for nanoimprint lithography. The mold used for nanoimprinting had a periodic grating structure with a period of 320 nm, a comb height of 25 nm, and a comb width-to-structure period ratio of 0.48. The perovskite film, together with the mold, was positioned in a laboratory press, where a pressure of approximately 200 MPa was applied for 10 min. Following the removal of the mold, the substrate with the imprinted perovskite film underwent annealing at 90 °C for an additional 10 min within the controlled atmosphere of the dry N$_2$ glovebox.

Optical Measurements. *Angle-Resolved Spectroscopy.* Angle-resolved spectroscopy measurements were conducted using a 4F setup with a back-focal plane (BFP). This setup incorporated a slit spectrometer coupled to an imaging EMCCD camera (Andor Technologies Kymera 328i-B1 + Newton EMCCD DU970P-BVF) and a halogen lamp, which was connected to an optical fiber via a collimation lens for white light illumination. To facilitate excitation and signal collection, we employed a Mitutoyo Plan Apo Infinity Corrected objective with a 10× magnification and a numerical aperture of 0.28. Spatial filtering was executed within the intermediate image plane (IP) as it passed through the 4f scheme. Angle-resolved photoluminescence measurements were carried out in the same setup, utilizing a femtosecond laser with a tunable wavelength having a repetition rate of 1 kHz, and a width of 200 fs. The laser system featured a mode-locked Ti:sapphire laser operating at 800 nm, initially serving as a seed pulse for the regenerative amplifier (Spectra Physics, Spitfire Pro). It was further frequency-doubled through a BBO crystal to achieve a 400 nm wavelength or coupled with an optical parametric amplifier to obtain other pump wavelengths (Light Conversion, OPA). To achieve a pump spot of approximately 50 μm, a lens with a focal length of 1,000 mm was used to focus the laser beam in the BFP. In the collection channel, a CCD camera (Thorlabs 1.6 MP Color CMOS Camera DCC1645C) was employed, with a 150 mm tube lens positioned after the beam splitter. This camera facilitated imaging in both real and Fourier spaces.

Transient Transmission Spectroscopy. The TTS measurements were conducted using Newport's Transient Absorption Spectrometer. The laser beam for this setup was split into two components: a low-intensity probe pulse and a high-intensity pump pulse. The low-intensity pulse was passed through a motorized delay line and a half-wave plate, which allowed for control over its polarization. Subsequently, it reached a sapphire crystal, generating spectrally uniform white pulses. This white probe pulse is directed through the perovskite metasurface and onward to the spectrometer, where transmission spectra are recorded.

Conversely, the high-intensity pump pulse followed different paths based on the desired wavelength range. For measurements at a pump wavelength of 400 nm, the high-intensity pulse traversed a BBO crystal. For pump wavelengths in the range of 470−520 nm, the pulse was directed to the TTS system. To control the intensity of the pumping laser, we employed a gradient-neutral density filter was employed. The laser beam then passed through a chopper and was focused onto the sample. The TTS results were acquired by adjusting the delay line to vary the temporal delay between the pump and probe pulses.

Numerical Simulations. To perform numerical simulations of eigenmode spectra, we utilized the finite element method (FEM) solver within COMSOL Multiphysics, specifically in the frequency domain. We simulated the near-field distributions and resonant wavelengths using the eigenmode solver within COMSOL Multiphysics. All of these calculations were conducted for a metasurface positioned on a semi-infinite substrate, enclosed by a perfectly matched layer to mimic an infinite region. The simulation encompassed the unit cell extended to an infinite metasurface through the application of Bloch boundary conditions.

For the simulations of angle-resolved reflection spectra, a custom-written code utilizing the Fourier modal method, was employed.[66]

This method entails expanding the electromagnetic field and permittivity function into a Fourier series. The reflectance is computed by solving the wave equation within the discretized Fourier space while adhering to the appropriate boundary conditions. The efficiency of this approach was augmented through the utilization of adaptive coordinates, enabling us to attain a relative error of 10^{-4} by considering eight Fourier harmonics in the expansion.

ASSOCIATED CONTENT

Data Availability Statement

The data that support the findings of this study are available from the corresponding author upon reasonable request.

Supporting Information

The Supporting Information is available free of charge at https://pubs.acs.org/doi/10.1021/acsnano.3c10636.

> AFM of the perovskite metasurface, angle-resolved PL spectrum at room temperature with extracted and fitted exciton−polariton dispersion; angle-resolved PL spectrum with uncoupled PL; results of the TTS in the linear regime; comparison table and plots of the obtained all-optical transmission modulation with literature data; extended TTS data for different pump fluence at 400 nm pump wavelength; extracted polariton mode blueshift time scale; extended TTS data for different pump wavelength; rescaled TTS data with attention to the absorption band near $\Delta t = 0$; extended TTS data at exciton wavelength in comparison with the TTS data at condensate wavelength (PDF)

AUTHOR INFORMATION

Corresponding Authors

Hilmi Volkan Demir − *UNAM-Institute of Materials Science and Nanotechnology, National Nanotechnology Research Center, Department of Electrical and Electronics Engineering, Department of Physics, Bilkent University, Ankara 06800, Turkey; LUMINOUS! Center of Excellence for Semiconductor Lighting and Displays, School of Electrical and Electronic Engineering, School of Physical and Mathematical Sciences, School of Materials Science and Engineering, Nanyang Technological University, 639798, Singapore;* orcid.org/0000-0003-1793-112X; Email: hvdemir@ntu.edu.sg, volkan@bilkent.edu.tr

Sergey V. Makarov − *Qingdao Innovation and Development Center, Harbin Engineering University, Qingdao, Shandong 266000, China;* orcid.org/0000-0002-9257-6183; Email: s.makarov@metalab.ifmo.ru

Authors

Mikhail A. Masharin − *UNAM-Institute of Materials Science and Nanotechnology, National Nanotechnology Research Center, Department of Electrical and Electronics Engineering, Department of Physics, Bilkent University, Ankara 06800, Turkey; Laboratory of Bionanophotonic, Institute of Bioengineering, Lausanne 1015, Switzerland*

Tatiana Oskolkova − *UNAM-Institute of Materials Science and Nanotechnology, National Nanotechnology Research Center, Department of Electrical and Electronics Engineering, Department of Physics, Bilkent University, Ankara 06800, Turkey*

Furkan Isik − *UNAM-Institute of Materials Science and Nanotechnology, National Nanotechnology Research Center, Department of Electrical and Electronics Engineering,*

Department of Physics, Bilkent University, Ankara 06800, Turkey; orcid.org/0000-0001-5881-5438

Anton K. Samusev − *Experimentelle Physik 2, Technische Universität Dortmund, Dortmund 44227, Germany;* orcid.org/0000-0002-3547-6573

Complete contact information is available at:
https://pubs.acs.org/10.1021/acsnano.3c10636

Notes

The authors declare no competing financial interest.

REFERENCES

(1) Haffner, C.; Chelladurai, D.; Fedoryshyn, Y.; Josten, A.; Baeuerle, B.; Heni, W.; Watanabe, T.; Cui, T.; Cheng, B.; Saha, S.; et al. others Low-loss plasmon-assisted electro-optic modulator. *Nature* **2018**, *556*, 483−486.

(2) Messner, A.; Moor, D.; Chelladurai, D.; Svoboda, R.; Smajic, J.; Leuthold, J. Plasmonic, photonic, or hybrid? Reviewing waveguide geometries for electro-optic modulators. *APL Photonics* **2023**, *8*, 100901 DOI: 10.1063/5.0159166.

(3) Koos, C.; Vorreau, P.; Vallaitis, T.; Dumon, P.; Bogaerts, W.; Baets, R.; Esembeson, B.; Biaggio, I.; Michinobu, T.; Diederich, F.; et al. others All-optical high-speed signal processing with silicon−organic hybrid slot waveguides. *Nat. Photonics* **2009**, *3*, 216−219.

(4) Caulfield, H. J.; Dolev, S. Why future supercomputing requires optics. *Nat. Photonics* **2010**, *4*, 261−263.

(5) Zasedatelev, A. V.; Baranikov, A. V.; Sannikov, D.; Urbonas, D.; Scafirimuto, F.; Shishkov, V. Y.; Andrianov, E. S.; Lozovik, Y. E.; Scherf, U.; Stöferle, T.; et al. others Single-photon nonlinearity at room temperature. *Nature* **2021**, *597*, 493−497.

(6) Ishikawa, H. *Ultrafast all-optical signal processing devices*; John Wiley & Sons, 2008.

(7) Wabnitz, S.; Eggleton, B. J. All-optical signal processing. *Springer Series in Optical Sciences* **2015**, *194*. DOI: 10.1007/978-3-319-14992-9

(8) Pop, E. Energy dissipation and transport in nanoscale devices. *Nano Research* **2010**, *3*, 147−169.

(9) Grinblat, G.; Berté, R.; Nielsen, M. P.; Li, Y.; Oulton, R. F.; Maier, S. A. Sub-20 fs all-optical switching in a single Au-Clad Si nanodisk. *Nano Lett.* **2018**, *18*, 7896−7900.

(10) Rotenberg, N.; Caspers, J. N.; van Driel, H. M. Tunable ultrafast control of plasmonic coupling to gold films. *Phys. Rev. B* **2009**, *80*, 245420.

(11) MacDonald, K. F.; Sámson, Z. L.; Stockman, M. I.; Zheludev, N. I. Ultrafast active plasmonics. *Nat. Photonics* **2009**, *3*, 55−58.

(12) Baida, H.; Mongin, D.; Christofilos, D.; Bachelier, G.; Crut, A.; Maioli, P.; Del Fatti, N.; Vallée, F. Ultrafast Nonlinear Optical Response of a Single Gold Nanorod near Its Surface Plasmon Resonance. *Phys. Rev. Lett.* **2011**, *107*, No. 057402.

(13) Afinogenov, B. I.; Bessonov, V. O.; Soboleva, I. V.; Fedyanin, A. A. Ultrafast All-Optical Light Control with Tamm Plasmons in Photonic Nanostructures. *ACS Photonics* **2019**, *6*, 844−850.

(14) Yang, J.; Zhang, X. Optical Fiber Delivered Ultrafast Plasmonic Optical Switch. *Adv. Sci.* **2021**, *8*, 2100280.

(15) Fu, Y.; Song, Z.; Jiang, M.; Ma, H.; Lopez, R.; Wang, J.; Li, Y.; Zhang, X. Plasmonic Hot-Electron Injection Driving Ultrafast Phase Transition in Self-Supported VO2 Films for All-Optical Modulation. *ACS Photonics* **2022**, *9*, 3950−3957.

(16) Wurtz, G. A.; Pollard, R.; Hendren, W.; Wiederrecht, G. P.; Gosztola, D. J.; Podolskiy, V. A.; Zayats, A. V. Designed ultrafast optical nonlinearity in a plasmonic nanorod metamaterial enhanced by nonlocality. *Nat. Nanotechnol.* **2011**, *6*, 107−111.

(17) Kuznetsov, A. I.; Miroshnichenko, A. E.; Brongersma, M. L.; Kivshar, Y. S.; Luk'yanchuk, B. Optically resonant dielectric nanostructures. *Science* **2016**, *354*, aag2472.

(18) Li, G.; Zhang, S.; Zentgraf, T. Nonlinear photonic metasurfaces. *Nature Reviews Materials* **2017**, *2*, 1−14.

(19) Hu, X.; Jiang, P.; Ding, C.; Yang, H.; Gong, Q. Picosecond and low-power all-optical switching based on an organic photonic-bandgap microcavity. *Nat. Photonics* **2008**, *2*, 185−189.

(20) Dani, K. M.; Ku, Z.; Upadhya, P. C.; Prasankumar, R. P.; Brueck, S. R. J.; Taylor, A. J. Subpicosecond Optical Switching with a Negative Index Metamaterial. *Nano Lett.* **2009**, *9*, 3565−3569.

(21) Makarov, S.; Kudryashov, S.; Mukhin, I.; Mozharov, A.; Milichko, V.; Krasnok, A.; Belov, P. Tuning of magnetic optical response in a dielectric nanoparticle by ultrafast photoexcitation of dense electron−hole plasma. *Nano Lett.* **2015**, *15*, 6187−6192.

(22) Shcherbakov, M. R.; Vabishchevich, P. P.; Shorokhov, A. S.; Chong, K. E.; Choi, D.-Y.; Staude, I.; Miroshnichenko, A. E.; Neshev, D. N.; Fedyanin, A. A.; Kivshar, Y. S. Ultrafast All-Optical Switching with Magnetic Resonances in Nonlinear Dielectric Nanostructures. *Nano Lett.* **2015**, *15*, 6985−6990.

(23) Wu, R.; Collins, J.; Chekulaev, D.; Kaplan, A. All-Optical Modulation and Ultrafast Switching in MWIR with Sub-Wavelength Structured Silicon. *Appl. Sci.* **2019**, *9*, 1808.

(24) Shcherbakov, M. R.; Liu, S.; Zubyuk, V. V.; Vaskin, A.; Vabishchevich, P. P.; Keeler, G.; Pertsch, T.; Dolgova, T. V.; Staude, I.; Brener, I.; Fedyanin, A. A. Ultrafast all-optical tuning of direct-gap semiconductor metasurfaces. *Nat. Commun.* **2017**, *8*, 1−6.

(25) Pogna, E. A. A.; Celebrano, M.; Mazzanti, A.; Ghirardini, L.; Carletti, L.; Marino, G.; Schirato, A.; Viola, D.; Laporta, P.; De Angelis, C.; Leo, G.; Cerullo, G.; Finazzi, M.; Della Valle, G. Ultrafast, All Optically Reconfigurable, Nonlinear Nanoantenna. *ACS Nano* **2021**, *15*, 11150−11157.

(26) Fang, Y.; Yang, J.; Xiao, Z.; Zhang, J.; Chen, Y.; Wu, Q.; Song, Y. Ultrafast all-optical modulation in Fe-doped GaN at 1.31 and 1.55 μm with high contrast and ultralow power. *Appl. Phys. Lett.* **2017**, *110*, 161902 DOI: 10.1063/1.4980090.

(27) Grinblat, G.; Zhang, H.; Nielsen, M. P.; Krivitsky, L.; Berté, R.; Li, Y.; Tilmann, B.; Cortés, E.; Oulton, R. F.; Kuznetsov, A. I.; Maier, S. A. Efficient ultrafast all-optical modulation in a nonlinear crystalline gallium phosphide nanodisk at the anapole excitation. *Sci. Adv.* **2020**, *6*. DOI: 10.1126/sciadv.abb3123

(28) Grinblat, G.; Nielsen, M. P.; Dichtl, P.; Li, Y.; Oulton, R. F.; Maier, S. A. Ultrafast sub−30-fs all-optical switching based on gallium phosphide. *Sci. Adv.* **2019**, *5*. DOI: 10.1126/sciadv.aaw3262

(29) Alam, M. Z.; De Leon, I.; Boyd, R. W. Large optical nonlinearity of indium tin oxide in its epsilon-near-zero region. *Science* **2016**, *352*, 795−797.

(30) Guo, Q.; Cui, Y.; Yao, Y.; Ye, Y.; Yang, Y.; Liu, X.; Zhang, S.; Liu, X.; Qiu, J.; Hosono, H. A Solution-Processed Ultrafast Optical Switch Based on a Nanostructured Epsilon-Near-Zero Medium. *Adv. Mater.* **2017**, *29*, 1700754.

(31) Reshef, O.; De Leon, I.; Alam, M. Z.; Boyd, R. W. Nonlinear optical effects in epsilon-near-zero media. *Nature Reviews Materials* **2019**, *4*, 535−551.

(32) Kuttruff, J.; Garoli, D.; Allerbeck, J.; Krahne, R.; De Luca, A.; Brida, D.; Caligiuri, V.; Maccaferri, N. Ultrafast all-optical switching enabled by epsilon-near-zero-tailored absorption in metal-insulator nanocavities. *Commun. Phys.* **2020**, *3*, 1−7.

(33) Jiang, H.; Zhao, Y.; Ma, H.; Wu, Y.; Chen, M.; Wang, M.; Zhang, W.; Peng, Y.; Leng, Y.; Cao, Z.; Shao, J. Broad-Band Ultrafast All-Optical Switching Based on Enhanced Nonlinear Absorption in Corrugated Indium Tin Oxide Films. *ACS Nano* **2022**, *16*, 12878−12888.

(34) Yang, Y.; Kelley, K.; Sachet, E.; Campione, S.; Luk, T. S.; Maria, J.-P.; Sinclair, M. B.; Brener, I. Femtosecond optical polarization switching using a cadmium oxide-based perfect absorber. *Nat. Photonics* **2017**, *11*, 390−395.

(35) Basiri, A.; Rafique, M. Z. E.; Bai, J.; Choi, S.; Yao, Y. Ultrafast low-pump fluence all-optical modulation based on graphene-metal hybrid metasurfaces. *Light Sci. Appl.* **2022**, *11*, 1−14.

(36) Li, W.; Chen, B.; Meng, C.; Fang, W.; Xiao, Y.; Li, X.; Hu, Z.; Xu, Y.; Tong, L.; Wang, H.; Liu, W.; Bao, J.; Shen, Y. R. Ultrafast All-Optical Graphene Modulator. *Nano Lett.* **2014**, *14*, 955−959.

(37) Popkova, A. A.; Chezhegov, A. A.; Rybin, M. G.; Soboleva, I. V.; Obraztsova, E. D.; Bessonov, V. O.; Fedyanin, A. A. Bloch Surface Wave-Assisted Ultrafast All-Optical Switching in Graphene. *Adv. Opt. Mater.* **2022**, *10*, 2101937.

(38) Paternò, G. M.; Moretti, L.; Barker, A. J.; Chen, Q.; Müllen, K.; Narita, A.; Cerullo, G.; Scotognella, F.; Lanzani, G. Pump−Push−Probe for Ultrafast All-Optical Switching: The Case of a Nano-graphene Molecule. *Adv. Funct. Mater.* **2019**, *29*, 1805249.

(39) Bae, S.; Nah, S.; Lee, D.; Sajjad, M.; Singh, N.; Kang, K. M.; Kim, S.; Kim, G.-J.; Kim, J.; Baik, H.; Lee, K.; Sim, S. Exciton-Dominated Ultrafast Optical Response in Atomically Thin PtSe2. *Small* **2021**, *17*, 2103400.

(40) Cheng, Y.; Hong, H.; Zhao, H.; Wu, C.; Pan, Y.; Liu, C.; Zuo, Y.; Zhang, Z.; Xie, J.; Wang, J.; Yu, D.; Ye, Y.; Meng, S.; Liu, K. Ultrafast Optical Modulation of Harmonic Generation in Two-Dimensional Materials. *Nano Lett.* **2020**, *20*, 8053−8058.

(41) Srivastava, Y. K.; Chaturvedi, A.; Manjappa, M.; Kumar, A.; Dayal, G.; Kloc, C.; Singh, R. MoS2 for Ultrafast All-Optical Switching and Modulation of THz Fano Metaphotonic Devices. *Adv. Opt. Mater.* **2017**, *5*, 1700762.

(42) Grinblat, G.; Abdelwahab, I.; Nielsen, M. P.; Dichtl, P.; Leng, K.; Oulton, R. F.; Loh, K. P.; Maier, S. A. Ultrafast All-Optical Modulation in 2D Hybrid Perovskites. *ACS Nano* **2019**, *13*, 9504−9510.

(43) Savvidis, P.; Baumberg, J.; Stevenson, R.; Skolnick, M.; Whittaker, D.; Roberts, J. Angle-resonant stimulated polariton amplifier. *Physical review letters* **2000**, *84*, 1547.

(44) Chen, W.; Kaya Özdemir, Ş.; Zhao, G.; Wiersig, J.; Yang, L. Exceptional points enhance sensing in an optical microcavity. *Nature* **2017**, *548*, 192−196.

(45) Özdemir, Ş. K.; Rotter, S.; Nori, F.; Yang, L. Parity−time symmetry and exceptional points in photonics. *Nature materials* **2019**, *18*, 783−798.

(46) Duggan, R.; Mann, S. A.; Alu, A. Limitations of sensing at an exceptional point. *ACS Photonics* **2022**, *9*, 1554−1566.

(47) Ardizzone, V.; Riminucci, F.; Zanotti, S.; Gianfrate, A.; Efthymiou-Tsironi, M.; Suàrez-Forero, D.; Todisco, F.; De Giorgi, M.; Trypogeorgos, D.; Gigli, G.; et al. Polariton Bose−Einstein condensate from a bound state in the continuum. *Nature* **2022**, *605*, 447−452.

(48) Grudinina, A.; Efthymiou-Tsironi, M.; Ardizzone, V.; Riminucci, F.; Giorgi, M. D.; Trypogeorgos, D.; Baldwin, K.; Pfeiffer, L.; Ballarini, D.; Sanvitto, D.; et al. Collective excitations of a bound-in-the-continuum condensate. *Nat. Commun.* **2023**, *14*, 3464.

(49) Masharin, M.; Samusev, A.; Bogdanov, A.; Iorsh, I.; Demir, H.; Makarov, S. Room-Temperature Exceptional-Point-Driven Polariton Lasing from Perovskite Metasurface. *Adv. Funct. Mater.* **2023**, *33*, 2215007.

(50) Alias, M. S.; Dursun, I.; Saidaminov, M. I.; Diallo, E. M.; Mishra, P.; Ng, T. K.; Bakr, O. M.; Ooi, B. S. Optical constants of CH3NH3PbBr3 perovskite thin films measured by spectroscopic ellipsometry. *Opt. Express* **2016**, *24*, 16586−16594.

(51) Yulaev, A.; Kim, S.; Li, Q.; Westly, D. A.; Roxworthy, B. J.; Srinivasan, K.; Aksyuk, V. A. Exceptional points in lossy media lead to deep polynomial wave penetration with spatially uniform power loss. *Nat. Nanotechnol.* **2022**, *17*, 583−589.

(52) Soufiani, A. M.; Huang, F.; Reece, P.; Sheng, R.; Ho-Baillie, A.; Green, M. A. Polaronic exciton binding energy in iodide and bromide organic-inorganic lead halide perovskites. *Appl. Phys. Lett.* **2015**, *107*, 231902.

(53) Masharin, M. A.; Shahnazaryan, V. A.; Benimetskiy, F. A.; Krizhanovskii, D. N.; Shelykh, I. A.; Iorsh, I. V.; Makarov, S. V.;

Samusev, A. K. Polaron-enhanced polariton nonlinearity in lead halide perovskites. *Nano Lett.* **2022**, *22*, 9092−9099.

(54) Masharin, M. A.; Shahnazaryan, V. A.; Iorsh, I. V.; Makarov, S. V.; Samusev, A. K.; Shelykh, I. A. Room-temperature polaron-mediated polariton nonlinearity in MAPbBr3 perovskites. *ACS Photonics* **2023**, *10*, 691−698.

(55) Lu, L.; Le-Van, Q.; Ferrier, L.; Drouard, E.; Seassal, C.; Nguyen, H. S. Engineering a light−matter strong coupling regime in perovskite-based plasmonic metasurface: quasi-bound state in the continuum and exceptional points. *Photonics Research* **2020**, *8*, A91−A100.

(56) Wei, J.-H.; Wang, X.-D.; Liao, J.-F.; Kuang, D.-B. High photoluminescence quantum yield (95%) of MAPbBr3 nanocrystals via reprecipitation from methylamine-MAPbBr3 liquid. *ACS Applied Electronic Materials* **2020**, *2*, 2707−2715.

(57) Zhang, M.; Yu, H.; Lyu, M.; Wang, Q.; Yun, J.-H.; Wang, L. Composition-dependent photoluminescence intensity and prolonged recombination lifetime of perovskite CH 3 NH 3 PbBr 3- x Cl x films. *Chem. Commun.* **2014**, *50*, 11727−11730.

(58) Ciuti, C.; Savona, V.; Piermarocchi, C.; Quattropani, A.; Schwendimann, P. Role of the exchange of carriers in elastic exciton-exciton scattering in quantum wells. *Phys. Rev. B* **1998**, *58*, 7926.

(59) Glazov, M.; Ouerdane, H.; Pilozzi, L.; Malpuech, G.; Kavokin, A.; d'Andrea, A. Polariton-polariton scattering in microcavities: A microscopic theory. *Phys. Rev. B* **2009**, *80*, 155306.

(60) Shan, H.; Iorsh, I.; Han, B.; Rupprecht, C.; Knopf, H.; Eilenberger, F.; Esmann, M.; Yumigeta, K.; Watanabe, K.; Taniguchi, T.; et al. Brightening of a dark monolayer semiconductor via strong light-matter coupling in a cavity. *Nat. Commun.* **2022**, *13*, 1−7.

(61) Masharin, M. A.; Khmelevskaia, D.; Kondratiev, V. I.; Markina, D. I.; Utyushev, A. D.; Dolgintsev, D. M.; Dmitriev, A. D.; Shahnazaryan, V. A.; Pushkarev, A. P.; Isik, F.; Iorsh, I. V.; Shelykh, I. A.; Demir, H. V.; Samusev, A. K.; Makarov, S. V. Polariton lasing in Mie-resonant perovskite nanocavity. *arXiv:2305.12973*, 2023.

(62) Feng, J.; Wang, J.; Fieramosca, A.; Bao, R.; Zhao, J.; Su, R.; Peng, Y.; Liew, T. C.; Sanvitto, D.; Xiong, Q. All-optical switching based on interacting exciton polaritons in self-assembled perovskite microwires. *Science. Advances* **2021**, *7*, eabj6627.

(63) Brichkin, A.; Novikov, S.; Larionov, A.; Kulakovskii, V.; Glazov, M.; Schneider, C.; Höfling, S.; Kamp, M.; Forchel, A. Effect of Coulomb interaction on exciton-polariton condensates in GaAs pillar microcavities. *Phys. Rev. B* **2011**, *84*, 195301.

(64) Pick, A.; Zhen, B.; Miller, O. D.; Hsu, C. W.; Hernandez, F.; Rodriguez, A. W.; Soljačić, M.; Johnson, S. G. General theory of spontaneous emission near exceptional points. *Opt. Express* **2017**, *25*, 12325−12348.

(65) Tatarinov, D. A.; Anoshkin, S. S.; Tsibizov, I. A.; Sheremet, V.; Isik, F.; Zhizhchenko, A. Y.; Cherepakhin, A. B.; Kuchmizhak, A. A.; Pushkarev, A. P.; Demir, H. V.; et al. High-Quality CsPbBr3 Perovskite Films with Modal Gain above 10 000 cm- 1 at Room Temperature. *Advanced Optical Materials* **2023**, *11*, 2202407.

(66) Vallius, T.; Honkanen, M. Reformulation of the Fourier modal method with adaptive spatial resolution: application to multilevel profiles. *Opt. Express* **2002**, *10*, 24−34.